metals

MDPI

Article

Analysis of the Effect of Tungsten Inert Gas Welding Sequences on Residual Stress and Distortion of CFETR Vacuum Vessel Using Finite Element Simulations

Jingwen Zhang [1], Liming Yu [1,*], Yongchang Liu [1], Zongqing Ma [1], Huijun Li [1], Chenxi Liu [1], Jiefeng Wu [2], Jianguo Ma [2] and Zhanlun Li [3]

[1] State Key Lab of Hydraulic Engineering Simulation and Safety, Tianjin Key Lab of Composite and Functional Materials, Tianjin University, Tianjin 300072, China; jwzhang1993@163.com (J.Z.); ycliu@tju.edu.cn (Y.L.); zqma@tju.edu.cn (Z.M.); huijun@uow.edu.au (H.L.); cxliu@tju.edu.cn (C.L.)
[2] Institute of Plasma Physics, Chinese Academy of Science, Hefei 230031, China; wjf2013@163.com (J.W.); liming-y-h@263.net (J.M.)
[3] Science and Technology Company of Beijing Semboo, Beijing 101300, China; zlli2015@163.com
* Correspondence: lmyu@tju.edu.cn; Tel.: +86-1502-2781-376

Received: 8 October 2018; Accepted: 31 October 2018; Published: 6 November 2018

Abstract: The as-welded sectors of China Fusion Engineering Testing Reactor (CFETR) vacuum vessel (VV) have very tight tolerances. However, it is difficult to investigate the welding stress and distortion without the production of a full-scale prototype. Therefore, it is important to predict and reduce the welding stress and distortion to guarantee the final assembly by using an accurately adjusted finite element model. In this paper, a full-scale finite element model of the 1/32 VV mock-up was built by ABAQUS which is a powerful finite element software for engineering simulation, and three different tungsten inert gas (TIG) welding sequences were simulated to study the effect of welding sequences on the welding stress and distortion. The results showed that the main welding stress happened on the weld zone, and the maximum distortion occurred on the shell near the welding joints between the inboard segment (PS1) and the lower segment (PS4). The inboard segment (PS1), upper segment (PS2), and lower segment (PS4) distorted to inside of the shell perpendicularly, while the equatorial segment (PS3) distorted to outside of the shell perpendicularly. According to the further analysis, the maximum welding stresses in sequence 1, sequence 2, and sequence 3 were 234.509 MPa, 234.731 MPa, and 234.508 MPa, respectively, and the average welding stresses were 117.268 MPa, 117.367 MPa, and 117.241 MPa, respectively, meanwhile, the maximum welding displacements in sequence 1, sequence 2, and sequence 3 were 1.158 mm, 1.157 mm, and 1.149 mm, respectively, and the average welding displacements were 1.048 mm, 1.053 mm, and 1.042 mm, respectively. Thus, an optimized welding sequence 3 was obtained and could be applied to the practical assembly process of the 1/32 VV mock-up.

Keywords: welding sequence; welding stress; welding distortion; finite element simulation; CFETR

1. Introduction

China Fusion Engineering Testing Reactor (CFETR) is a superconducting Tokamak magnet which has an equivalent scale and function to the International Thermonuclear Experimental Reactor (ITER). The vacuum vessel (VV) plays a very important role in China Fusion Engineering Testing Reactor (CFETR) facility, and it has a double-walled torus-shaped structure which consists of inner shells, outer shells, poloidal ribs, toroidal ribs, and in-wall shielding [1]. The 1/32 VV mock-up of CFETR

is manufactured from four poloidal segments (PS), including inboard segment (PS1), upper segment (PS2), equatorial segment (PS3), and lower segment (PS4), as shown in Figure 1. In order to guarantee the final assembly with the other vacuum vessel sectors suitably, the overall profile of the 1/32 VV mock-up must have tight tolerances [2]. However, it is difficult to achieve a tight tolerance due to the nature of the austenitic steel 316LN (ITER Grade), which is chosen as the raw material of the CFETR vacuum vessel. The austenitic steel 316LN exhibits high welding stresses and distortions during the welding process because of its low thermal conductivity and high thermal expansion coefficient [3].

Welding stresses have a harmful influence on the quality of the as-welded structures, and usually lead to a failure of the welding joints [4]. At the same time, welding distortions could affect the final assembly of the whole structure and increase the production cost [5]. Thus, it is important to seek an effective way to predict, and reduce, the welding stresses and distortions.

In recent years, some studies have been carried out to predict and reduce the welding residual stresses and distortions using finite element models [6–12]. Bonakdar et al. [13] predicted the level of residual stresses, as well as distortions of the electron beam welded shrouds of Inconel-713LC gas turbine blades using finite element simulations. Kim et al. [14] investigated the effect of the phase transformation on the generation of welding distortions and stresses of LBW and HYBW using finite element simulation. Rong et al. [15] studied the deformation and residual stress of the laser welding 316L T-joint using finite element simulation. In addition, the optimization of welding sequences has become more popular for controlling welding stresses and distortions using finite element models. Fu et al. [16] studied the influence of welding sequences on the residual stress and distortion of fillet welded structures, and found that the welding deposition sequence significantly influenced the magnitude of stresses and the mode of deflections. Chen et al. [17] examined the influence of the welding sequence on the welding deformation and stress of a stiffened plate structure, and found that welding sequences influenced the magnitude of panel bending distortion and transverse stresses at the top surface of the plates. The effect of the welding sequences on welding distortions in pipes was examined by Sattari-Far [18], and indicated that the welding sequences affected the diameter variations in the pipes. Deng [19] determined the effect of deposition sequences on welding residual stresses and deformations in J-groove welded joint, and found that the deposition sequence had a significant influence on welding residual stresses distribution in the tube–block joint, meanwhile, the deposition sequence influenced not only the magnitude of distortions but also the deformation mode. All those studies indicated that welding sequences had an important effect on the welding residual stress and distortion. More recently, the influence of welding sequences on welding stresses and distortions has been investigated on the International Thermonuclear Experimental Reactor (ITER) vacuum vessel using finite element models. For example, the influence of electron-beam welding sequences on the ITER vacuum vessel prototype VATS was examined by Guirao et al. [20], and it was found that the distortion simulation could optimize the welding sequences to achieve tight tolerances and obtain low distortion components. Martín-Menéndez et al. [21] studied the influence of electron-beam welding sequences on ITER vacuum vessel for a fixed manufacturing route using finite element simulation, and observed that the welding sequences had a more significant influence in a lowly constrained assembly than in a highly constrained one. These studies have confirmed the accuracy and feasibility of the finite element simulation, and promoted the integration of theories and methodology systems. However, most of these studies focused on simple structures, but paid little attention to complex structures, such as the 1/32 VV of CFETR.

In this paper, in order to optimize the manufacture sequences of the 1/32 VV mock-up [22–24], three different welding sequences were applied to the finite element simulation. The finite element model was adjusted and validated on the coupon by comparing the simulated welding stress and distortion with experimental results. Then, the established finite element model was applied to the simulation of the 1/32 VV mock-up to predict the corresponding welding stress and distortion.

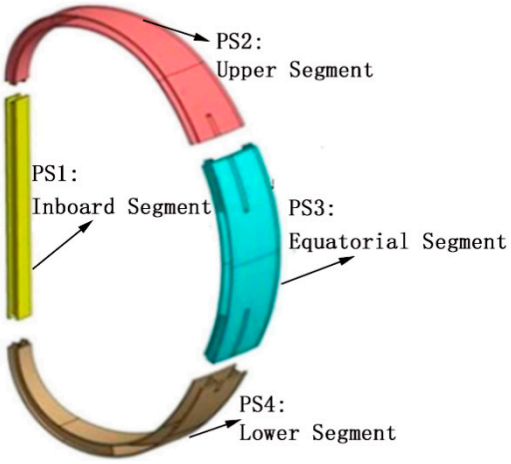

Figure 1. Assembly of the 1/32 vacuum vessel (VV) mock-up, including PS1 (inboard segment), PS2 (upper segment), PS3 (equatorial segment), and PS4 (lower segment).

2. Methodology Validation Using the Coupon

In order to ensure the accuracy and feasibility of the finite element model for large scale and complex structures, the finite element model was adjusted by comparing the experimental results with simulated results on the coupon. When the trend and magnitude of the welding stress and distortion in simulation were similar with those on experimental coupon, the finite element model was applied to the simulation of 1/32 VV mock-up.

2.1. Measurement of Welding Stresses and Distortions of the Coupon

The testing coupon was made of austenitic steel 316LN, with a length of 300 mm, a width of 300 mm and a thickness of 50 mm, as shown in Figure 2. Its chemical compositions are given in Table 1. In order to reduce the heat input, the narrow U-groove was chosen as the welding joint of the coupon (as shown in Figure 3a), and the whole joint was completed by about thirty weld beads. Considering the quality of the as-welded joint and the much larger width from the bottom to the top of the U-joint, the welding parameters need to be adjusted during the welding process. Therefore, after many tests about the welding process of the testing coupon, the U-joint was divided into four layers, and each layer includes several weld beads (as shown in Figure 3b), meanwhile, each layer has its own welding parameters. The whole welding process was completed by manual tungsten inert gas (TIG) welding, and the welding parameters of the four layers are listed in Table 2. In order to avoid the rigid displacement, four corners were fixed on the welding platform by spot welding before the coupon was welded, and released immediately after welding, as shown in Figure 2. Finally, the as-welded coupon was cooled in air.

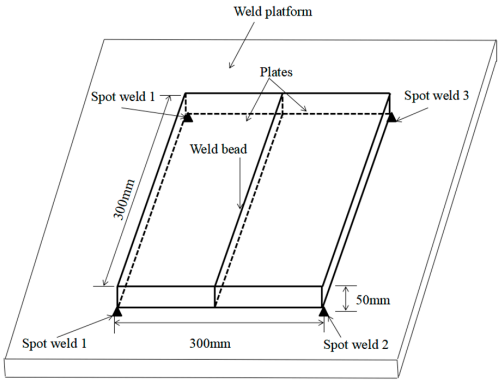

Figure 2. Diagram of the dimension and clamp conditions of the testing coupon.

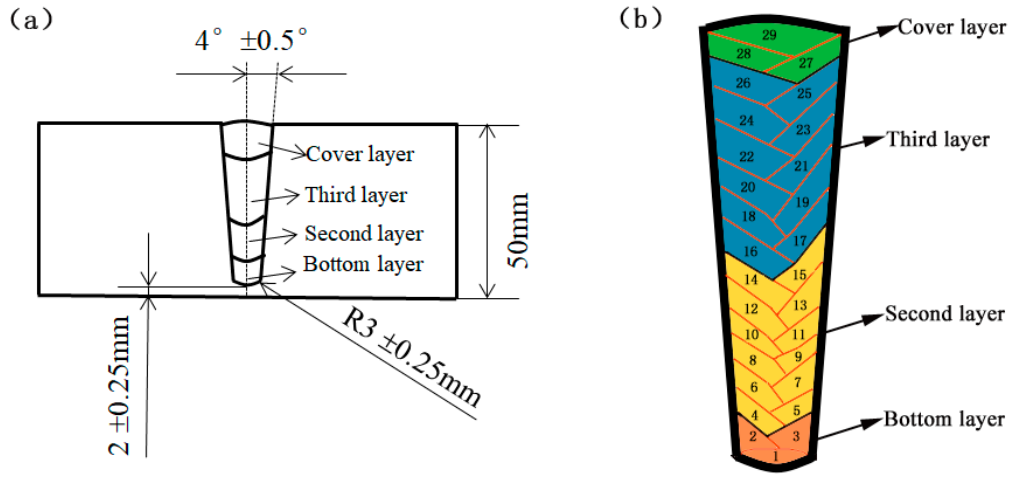

Figure 3. (**a**) Geometry of the U-groove; (**b**) all weld beads were divided into four layers: bottom layer, second layer, third layer, and cover layer.

Table 1. Chemical compositions of the austenitic steel 316LN (wt %).

C	Si	Mn	P	S	Cr	Mo	Ni	N	Cu
0.021	0.77	1.109	0.039	0.001	16.92	2.03	12.16	0.033	0.20

Table 2. Welding parameters of the four layers.

Layers	Current (A)	Voltage (V)	Speed (mm/min)
Bottom layer	70	10	100
Second layer	160	12	80
Third layer	200	12	80
Cover layer	170	12	45

Welding residual stresses of the as-welded coupon were measured by X-ray diffraction (XRD) [25,26], and the equipment was iXRD which was made by Proto company in Canada. The basic principle is the crystal space will be changed under welding stresses. Meanwhile, the diffraction peak will drift when Bragg diffraction occurs, and the distance of drifting depends on the welding stress. According to the Bragg equation and the elastic theory, the principal residual stress could be calculated by the following equations:

$$\sigma = K \bullet M, \tag{1}$$

$$M = \frac{\partial(2\theta)}{\partial(\sin^2 \psi)}, \tag{2}$$

$$K = -\frac{E}{2(1+\upsilon)} Ctg\theta_0 \bullet \frac{\pi}{180}, \tag{3}$$

where parameter σ is the principal stress, K is the stress coefficient, M is the slope of the function of $2\theta - \sin^2 \psi$, θ is the diffraction angle, ψ is the angle between the normal of the coupon surface and the normal of the diffraction crystal face, E is the elastic modulus, υ is the Poisson ratio, and θ_0 is the diffraction angle without stresses. In the test, ψ were defined as 11.4°, 5.5°, 0°, -9.02°, -13.6°, -18.18°, -27.2°, -32.7°, and -38.6°, E was 196,000 N/m^2, υ was 0.3, and θ_0 was 152.3°. Meanwhile, the apparatus is shown in Figure 4a. The voltage was 20 KV, the current was 4 mA, the exposure time was 10 s, and the spot size was 3 mm. Six checkpoints were selected at the upper surface of the coupon to compare with simulated results, as marked in Figure 4b.

Welding residual distortions were measured by a digital caliper, as shown in Figure 5a. Eleven checkpoints were selected at the upper surface of the coupon to compare with the simulated vertical

deformation, as shown in Figure 5b. The detailed measured process was as follows (as shown in Figure 5c): (1) measuring the distance between the bottom surface and horizontal line, d_1; (2) measuring the distance between the bottom surface and the upper surface, d_2; (3) vertical distortion $Z = d_1 - d_2$.

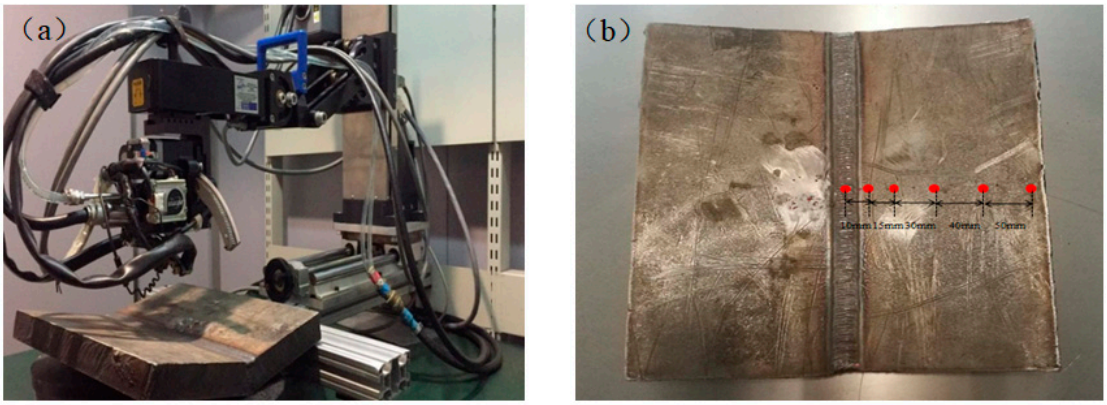

Figure 4. (**a**) The apparatus of measuring the actual stress; (**b**) 6 positions (marked as red points) for stress measurements.

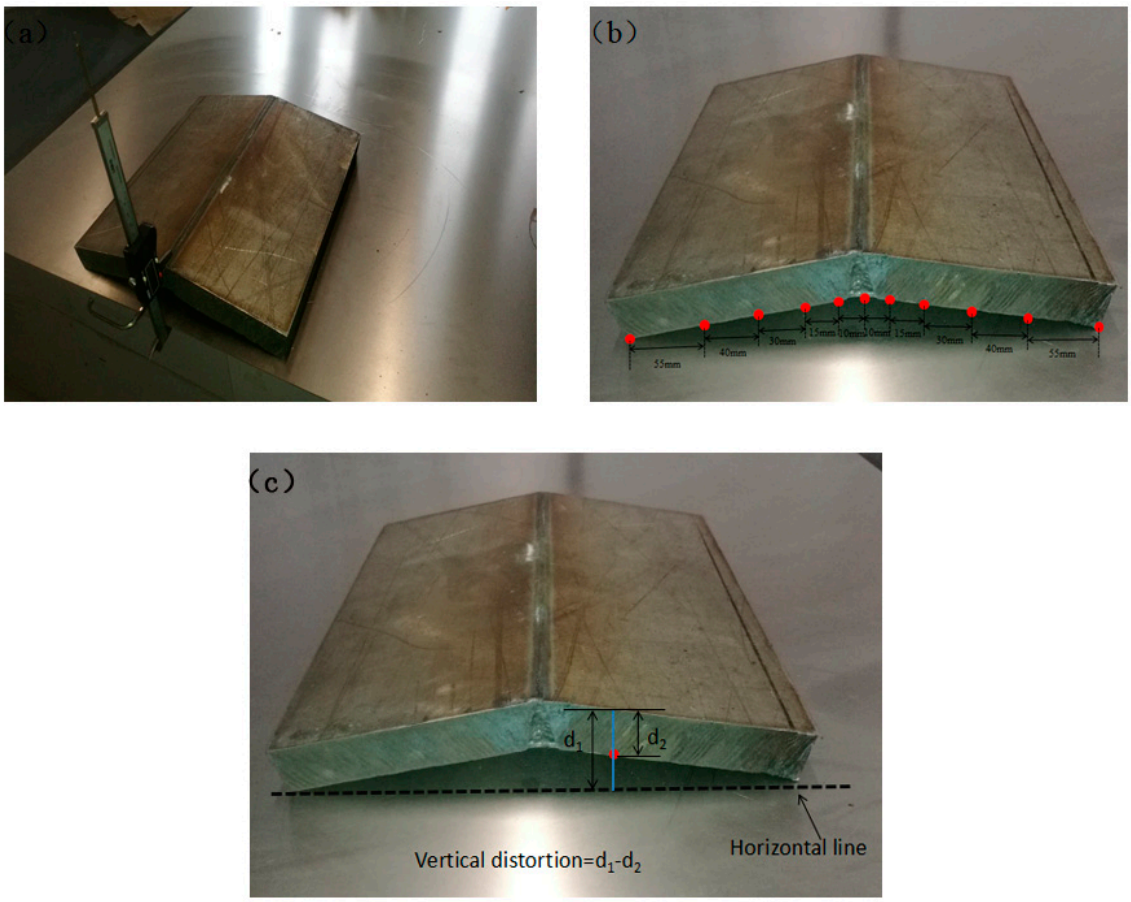

Figure 5. (**a**) The apparatus of measuring the actual distortion; (**b**) 11 positions (marked as red points) for distortions measurement; (**c**) the detailed measurement method of vertical distortions.

2.2. Simulation of Welding Stresses and Distortions of the Coupon

In order to ensure the accuracy of calculation results and consider the interaction between temperature and stress, the direct coupled thermo-elasto-plastic approach was used in the simulation,

as shown in Figure 6, in which the distribution of temperature field, stress field, and distortion field could be obtained synchronously.

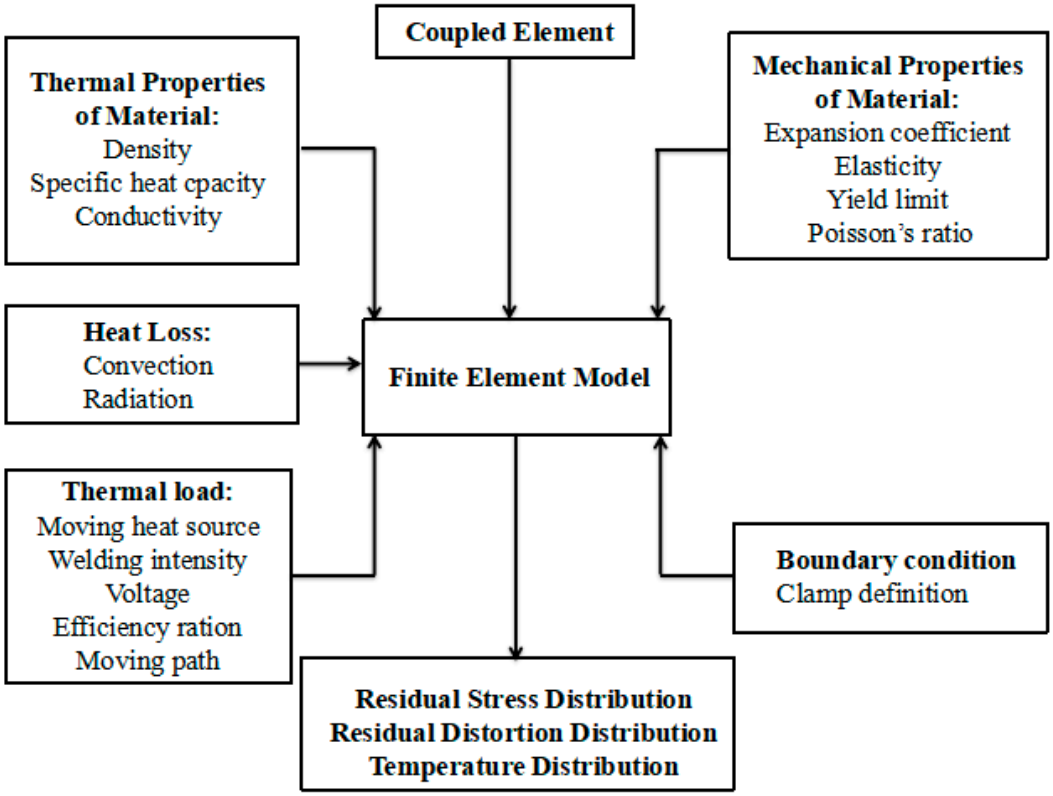

Figure 6. Flow diagram of the direct coupled thermo-elasto-plastic approach.

2.2.1. Finite Element Model

A full-size finite element model of the coupon, which includes 55920 meshes and 61183 nodes, was built using an 8-node thermally coupled element C3D8T by ABAQUS 2017 which was developed by Dassault company in America, as shown in Figure 7. Similarly, in order to avoid rigid displacement, four corner points (a, b, c, and d) were selected as the restriction conditions, of which a point was constrained in *X*, *Y*, and *Z* directions, b point was constrained in *X* and *Y* directions, and c point and d point were constrained in *Y* direction. Mesh refinement was applied to the welding joint (as marked by the red circle in Figure 8a) because the computation cost would be inevitably high if all meshes had the same size. Meanwhile, the mesh sizes have an important effect on simulated results of the proposed finite element model, and Lorza et al. [27] studied the mesh sizes that a proposed finite element model requires, so that the difference between the simulated results and experiments is small. The mesh sizes used in the finite element model were 2 mm for the weld metal, 20 mm for the base metal, and 5 mm and 10 mm for the transitional region between the weld metal and the base metal, as shown in Figure 8c. Moreover, in order to keep the consistency between the simulation and the practical welding, the welding joint was completed by twenty-nine weld beads and divided into four weld layers (as shown in Figure 8b) in the simulation. The simulation parameters of each layer were defined according to the practical welding parameters.

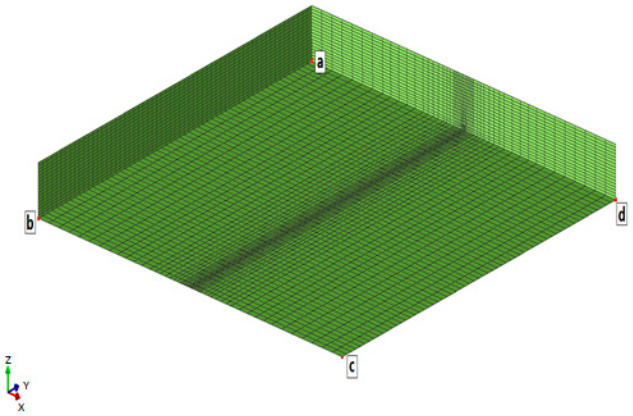

Figure 7. The finite element model and restriction points (a, b, c, and d) of the coupon (a point was constrained in *X*, *Y*, and *Z* directions, b point was constrained in *X* and *Y* directions, c and d points were constrained in *Y* direction).

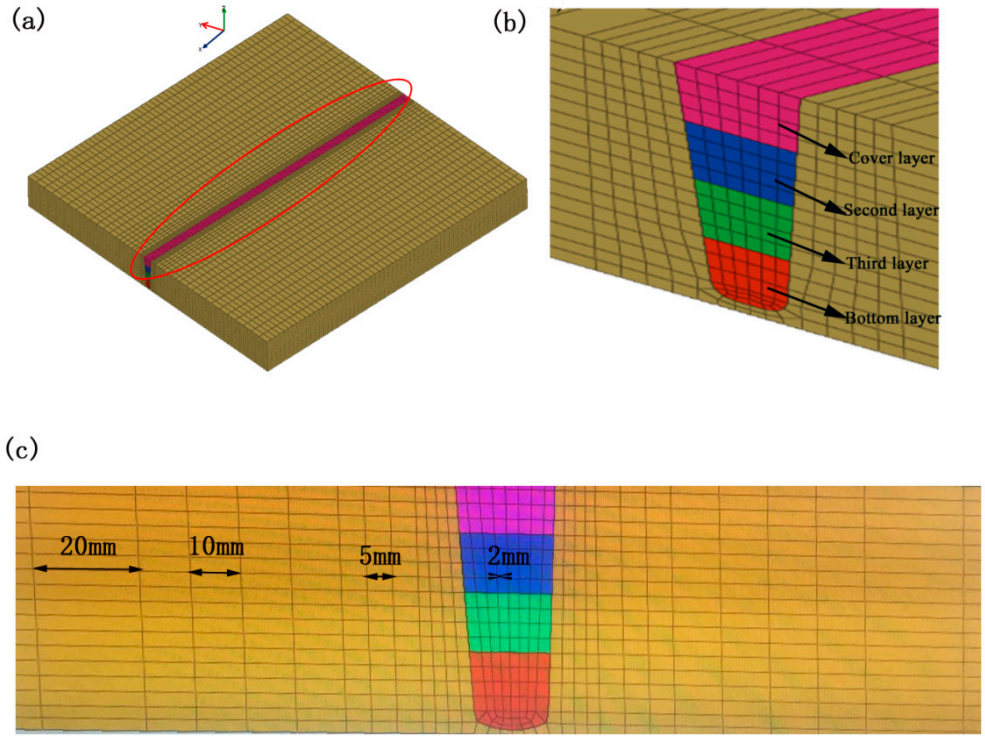

Figure 8. (**a**) Mesh refinement for the weld region of the coupon (the red circle); (**b**) four weld layers of the welding joint represented by four colors; (**c**) the mesh sizes used in the finite element model.

2.2.2. Material Model

Table 3 shows the thermal and mechanical properties of the austenitic steel 316LN, and all thermal and mechanical properties are strongly temperature-dependent. von Mises yield function was used as the yield criterion, and Voce's hardening equation was used as the hardening law.

Table 3. The thermal and mechanical properties of the austenitic steel 316LN.

T (K)	S_u (MPa)	$S_{y_{0.2}}$ (MPa)	ν	E (N/m^2)	α (1/K)	ρ (kg/m^3)	K (W/mk)	C (J/kg K)
293	525	271	0.3	1.920×10^{11}	1.59×10^{-5}	7966	13.94	470
373	509	220	0.3	1.860×10^{11}	1.64×10^{-5}	7932	15.08	486
473	473	184	0.3	1.780×10^{11}	1.70×10^{-5}	7889	16.52	508
573	456	164	0.3	1.700×10^{11}	1.75×10^{-5}	7846	17.95	529
673	449	148	0.3	1.610×10^{11}	1.79×10^{-5}	7803	19.39	550
773	443	140	0.3	1.530×10^{11}	1.83×10^{-5}	7760	20.82	571
873	391	134	0.3	1.450×10^{11}	1.87×10^{-5}	7717	22.25	592
973	274	131	0.3	1.370×10^{11}	1.90×10^{-5}	7674	23.69	613
1273	170	116	0.3	1.168×10^{11}	1.98×10^{-5}	7516	25.13	676
1473	86	62	0.3	4.000×10^{10}	2.11×10^{-5}	7412	26.55	722
1673	24	19	0.3	5.000×10^{8}	2.35×10^{-5}	7297	27.99	761
1873	5	2	0.3	1.000×10^{7}	2.60×10^{-5}	7180	29.44	810

(T temperature, S_u ultimate tensile strength, $S_{y_{0.2}}$ yield stress, ν Poisson's ratio, E modulus of elasticity, α expansion coefficient, ρ density, K thermal conductivity, C special heat).

2.2.3. Heat Source Model

The model of the moving heat source plays an important role in the simulation of the welding process. In this study, a 3D-double ellipsoidal model, proposed by Goldak [28], was adopted to this simulation, as shown in Figure 9. At different times, the center of the heat source changed during the transient analysis. In the Cartesian coordinate system, the Y-axis was regarded as the welding direction. The first semi-ellipsoidal locates in the front of the welding arc, and the heat density equation is given by

$$Q_f(x_1, y_1, z_1) = 6\sqrt{3}\pi^{\frac{2}{3}} \frac{f_f \eta IV}{abc_f} \exp(-\frac{3x^2}{a^2} - \frac{3y^2}{{c_f}^2} - \frac{3z^2}{b^2}). \quad (4)$$

The second semi-ellipsoidal covers the remaining part of the welding arc, and the heat density equation is given by

$$Q_r(x_2, y_2, z_2) = 6\sqrt{3}\pi^{\frac{2}{3}} \frac{f_r \eta IV}{abc_r} \exp(-\frac{3x^2}{a^2} - \frac{3y^2}{{c_r}^2} - \frac{3z^2}{b^2}), \quad (5)$$

where f_f is the heat input proportion coefficients in the front part, f_r is the heat input proportion coefficients in the remaining part, I is the welding current, V is the welding voltage, η is the arc efficiency, and a, b, c_f, and c_r are the geometric parameters. Meanwhile, the parameters of the heat source model have great influence on the temperature field and the deformation field, and Lorza et al. [29] focused their work on the adjustment of the heat source parameters by genetic algorithms. In this simulation, the initial parameters of the heat source were defined according to the practical welding parameters, and then adjusted by comparing the experimental data with simulated results on the coupon. The finalized parameters of the heat source model in four weld layers has been shown in Table 4.

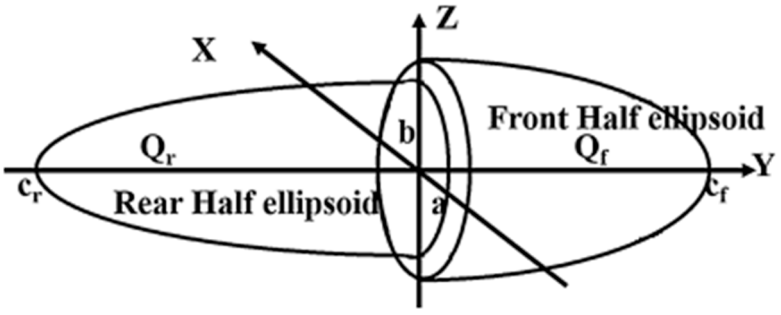

Figure 9. 3D-double ellipsoidal heat source used in the simulation.

Table 4. The finalized parameters of the heat source model in the simulation.

Parameters	Bottom Weld Layer	Second Weld Layer	Third Weld Layer	Cover Weld Layer
Heat source		3D-double ellipsoidal		
Velocity(mm/s)	1.667	1.333	1.333	0.75
Length (mm)	6	6.4	6.9	8
Width (mm)	5	4.9	5.2	6
Penetration(mm)	3	3.4	3.9	5
Energy (J/mm)	420	1440	1836	2720
Power ratio	1.2	1.2	1.2	1.2
Length ratio	0.5	0.5	0.5	0.5
Efficiency	0.9	0.9	0.9	0.9

2.2.4. Initial and Boundary Conditions

The welding process was conducted at room temperature, and the initial temperature was defined as 20 °C. The thermal convection and radiation between the coupon and the air were taken into account in this simulation, and governed by Newton's law of cooling and Stefan–Boltzmann relation as follows:

$$q_c = h(T_w - T_a), \tag{6}$$

$$q_r = \sigma\varepsilon({T_w}^4 - {T_a}^4), \tag{7}$$

where q_c and q_r are heat flux during convective and radiative losses, respectively ($W \bullet m^{-2}$), T_w and T_a are the surface and surrounding temperature, respectively (°C), h is the heat transfer coefficient for convection ($W \bullet m^{-2} \bullet K^{-1}$), σ is the Stefan–Boltzmann constant ($W \bullet m^{-2} \bullet K^{-4}$), and ε is emissivity. The finalized thermal convection coefficient was 10 $W \bullet m^{-2} \bullet K^{-1}$, and the finalized thermal radiation coefficient was 4.5 $W \bullet m^{-2} \bullet K^{-4}$.

2.3. Comparison between Experimental and Simulated Results

Figure 10 shows the colored map of the welding von Mises effective stress in simulation. As can be seen, the main stresses appear in the welding zone, and the stress values decrease gradually with increasing distance to the centerline of the welding zone. In order to compare experimental results with simulated results conveniently, route 1 (the black line as shown in Figure 10) at the upper surface of the colored map, was chosen to get the principal stress values in simulation, and 6 checkpoints were selected on the same route as route 1 on the coupon, to get experimental results. The principal stresses were analyzed according to the directions which were parallel (X direction) and perpendicular (Y direction) to the centerline of the welding joint.

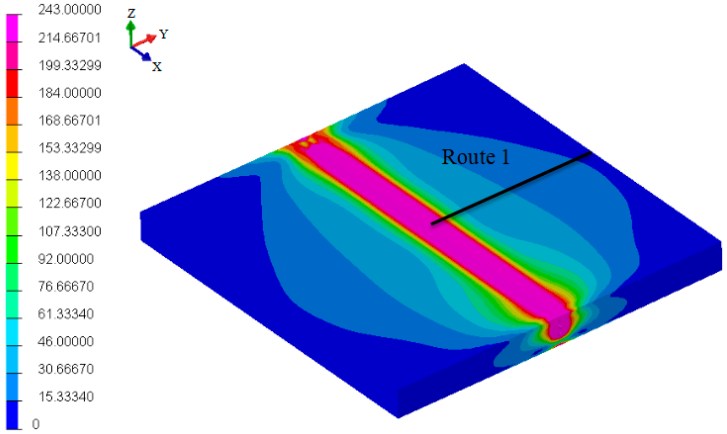

Figure 10. Colored map of the von Mises stress in simulation. The values on the left represent von Mises effective stress, where different colors indicate different stress values, and route 1 (black line) was chosen to compare the principal stress between simulation and experiment.

Figure 11 presents the comparison of the principal stresses. In the *Y* direction (as shown in Figure 11a), the compressive stress occurs in the welding zone and heat-affected zone, and it increases firstly, and then decreases to zero, in both the experiment and simulation, with increasing distance to the welding zone. In *X* direction (as shown in Figure 11b), the tensile stress occurs in the welding zone and heat-affected zone, and it increases firstly and, then, begins to decrease gradually in both the experiment and simulation. Finally, the stress varies from tensile to compressive with increasing distance to the welding zone, and tends to zero in the base metal. Overall, the trend and magnitude of the welding stress in simulation are consistent with that of experimental measurements.

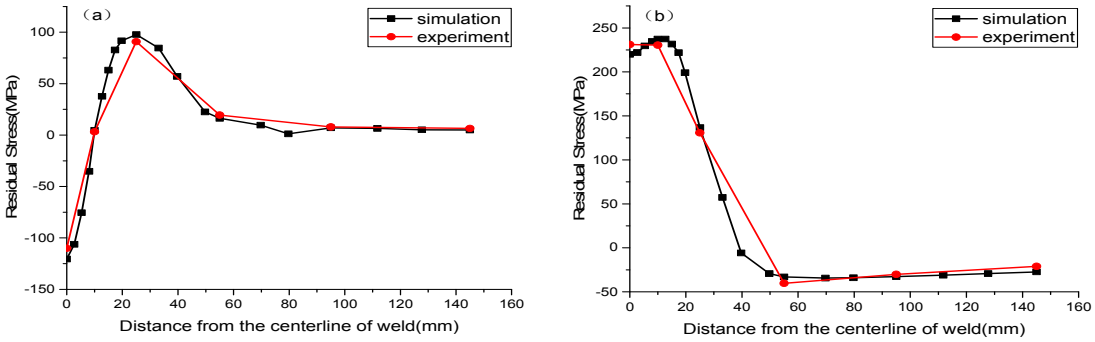

Figure 11. Comparison of the principal stresses between simulation and experiment. (**a**) The stresses in the *Y* direction (perpendicular to the welding direction); (**b**) the stresses in the *X* direction (parallel to the welding direction).

Table 5 shows the principal stress in *Y* direction obtained from the simulation and the experiment. The table indicates that the largest error between the simulated results and the experiment is 16.1%, and the smallest error is 6.5%. Meanwhile, Table 6 shows the principal stress in the *X* direction obtained from the simulation and the experiment. The largest error is 18.1%, and the smallest error is 3%.

Table 5. Values of the principal stresses in *Y* direction obtained from simulation and experiment.

Distance from the Centerline of the Weld Zone (mm)	Experimental (MPa)	Simulation (MPa)	Error (%)
0	−110.1	−120.5	9.4
10	4.3	4.67	8.6
25	90.82	97.7	7.6
55	19.45	16.3	16.1
95	7.98	7.06	11.5
145	4.6	4.9	6.5

Table 6. Values of the principal stresses in X direction obtained from simulation and experiment.

Distance from the Centerline of the Weld Zone (mm)	Experimental (MPa)	Simulation (MPa)	Error (%)
0	231.1	220	4.8
10	230.5	237.4	3
25	130.7	136.7	4.6
55	−40.3	−33	18.1
95	−30.1	−32.7	5.3
145	−25.0	−27.4	9.6

Figure 12 shows the colored map of the angular distortion in the *Z* direction in the simulation. As can be seen, an angular deformation occurs on the coupon, and the displacement increases with increasing distance to the centerline of the weld zone. In order to compare experimental results with simulated results conveniently, route 2 (the black line as shown in Figure 12) at the upper surface of the colored map was chosen to get the distortion values in the simulation, and 11 checkpoints were selected on the same route as route 2 on the coupon, to get experimental results.

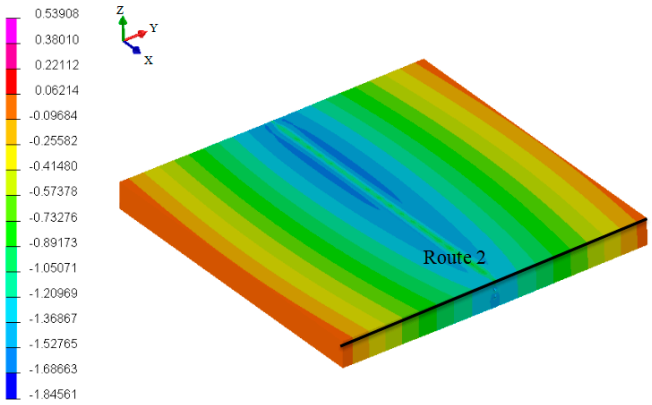

Figure 12. Colored map of the angular distortion in simulation. The values on the left represent the displacement, of which positive values indicate distortion in the positive direction of the *Z* axis and negative values indicate distortion in the negative direction of *Z* axis. Different colors indicate different distortion values, and route 2 (black line) was chosen to compare the displacement between simulation and experiment.

Figure 13 presents the comparison of the welding distortion. It is obvious that the angular deformation of the coupon happens in both the simulation and the experiment. The central part of the welding zone distorts to the positive direction of the *Z* axis because of extrusion, which is consistent with the variation of the welding stress, as mentioned above. The above comparison indicates that simulated results of the angular distortion show the same variation tend and magnitude with that in experiment.

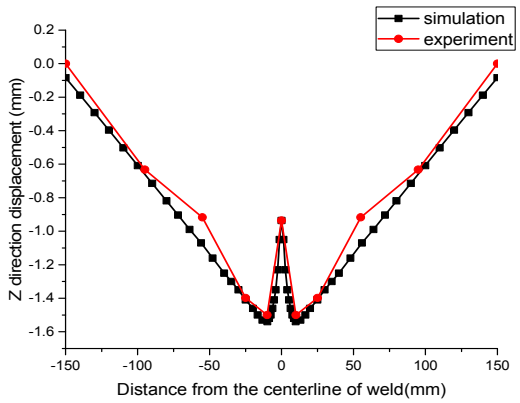

Figure 13. Comparison of the angular distortion in *Z* direction between simulation and experiment.

Table 7 shows the angular distortion obtained from the simulation and the experiment. The table indicates that the largest error is 18.7%, and the smallest error is 1.4%.

Table 7. Values of the angular distortion obtained from simulation and experiment.

Distance from the Centerline of Weld (mm)	Experimental (mm)	FEM (mm)	Error (%)
−150	−0.07	−0.0831	18.7
−95	−0.63	−0.608	3.5
−55	−0.92	−1.07	16.3
−25	−1.39	−1.41	1.4
−10	−1.50	−1.54	2.7
0	−0.92	−0.936	1.7
10	−1.50	−1.54	2.7
25	−1.38	−1.41	2.2
55	−0.93	−1.07	15.1
95	−0.62	−0.608	2.0
150	−0.07	−0.831	18.7

To sum up, the welding stresses and distortions showed identical variation trends and magnitudes between the simulated results and experiment by adjusting the finite element model on the coupon. The simulation methodology was validated, and the simulation parameters were finalized. Then, all could be applied to the simulation of three different welding sequences for the 1/32 VV mock-up.

3. Simulation of the 1/32 VV Mock-Up

3.1. Finite Element Model

A full-scale finite element model of the 1/32 VV mock-up, which includes 90,280 meshes and 135,988 nodes, was built by ABAQUS, as shown in Figure 14. In order to reduce the simulation time, mesh refinement was adopted on the welding joints (red circles in Figure 14). The simulation methodology, element types, heat source parameters, mesh sizes, and the parameters of convection and radiation, were all the same as those applied for the coupon, but the constraint conditions were set according to the practical production process (as shown in Figure 15), and all points were constrained in X, Y, and Z directions, as shown in Figure 16. The welding process included overhead welding, flat welding, and vertical welding, and the effect of gravity was ignored because the whole assembly process remained unchanged.

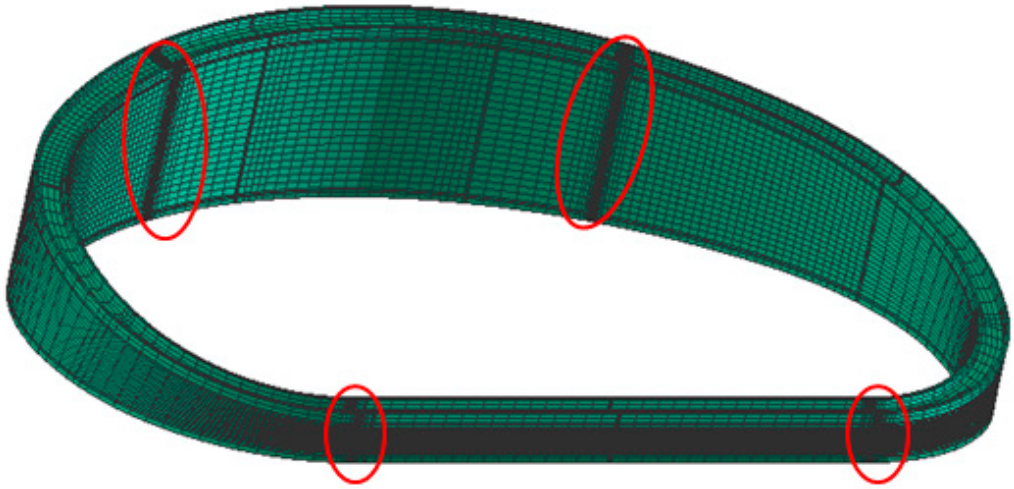

Figure 14. The full-size finite element model of the 1/32 VV mock-up, and the red circles represent the mesh refinement zones.

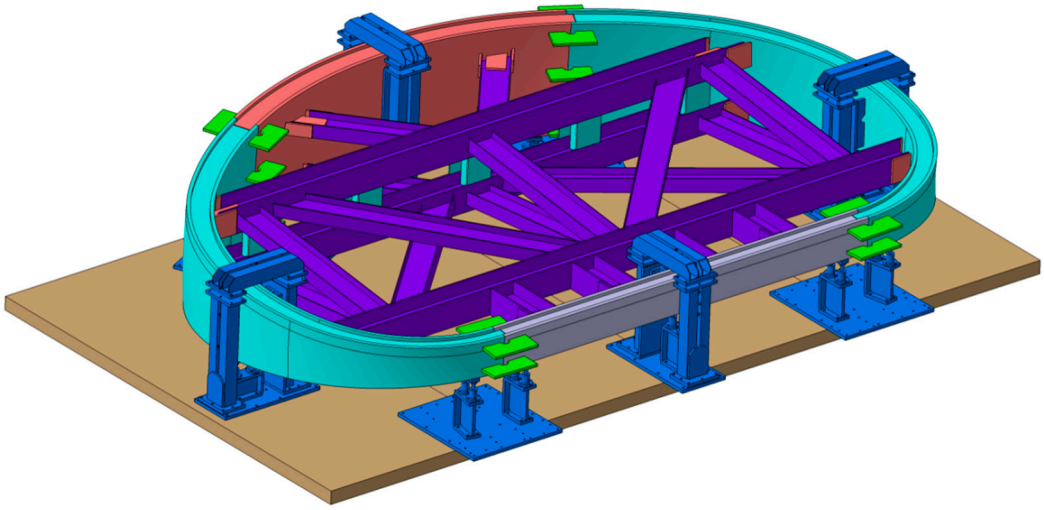

Figure 15. Constraint conditions in the practical production process of the 1/32 VV mock-up.

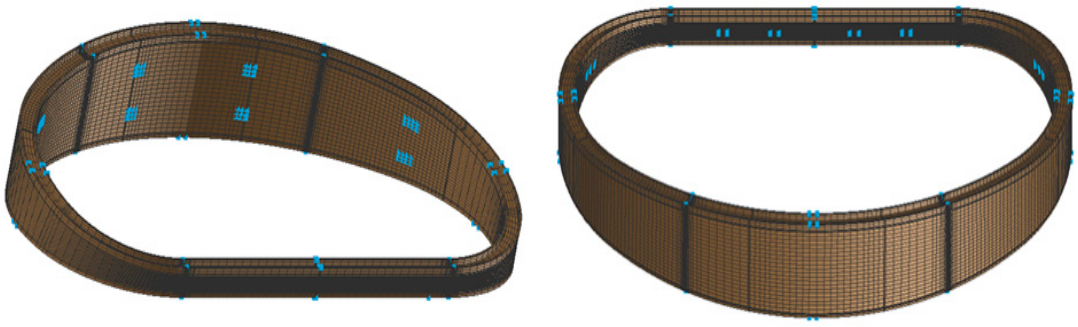

Figure 16. Constraints of the 1/32 VV mock-up in simulation. The blue points represent constrained points corresponding to the practical process, and every point was constrained in *X*, *Y*, and *Z* directions.

3.2. Welding Sequences

In order to investigate the effect of welding sequences on the welding stress and distortion, three different sequences were applied to the simulation of the 1/32 VV mock-up. The whole simulation process included 16 welding joints, totally, and each welding joint was accomplished by twenty-nine weld beads. For each joint, the outside weld was carried out first, and followed with the inside weld in simulation, due to the double-walled structure of the 1/32 VV.

Figure 17 shows the three welding sequences of the 1/32 VV mock-up. Every sequence was started at the joint between PS1 and PS2. Moreover, in every sequence, all bottom layers were carried out firstly, followed by the second layers, the third layers, and the cover layers, successively.

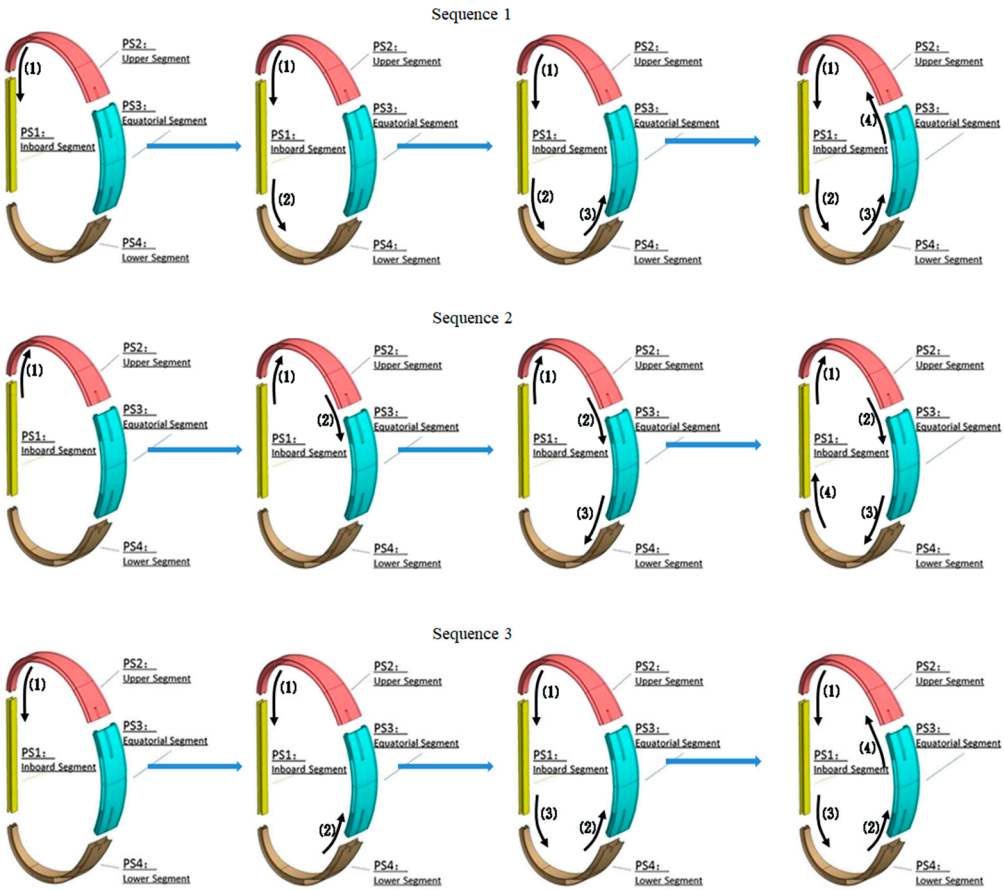

Figure 17. Three welding sequences of the 1/32 VV mock-up: welding anticlockwise in sequence 1, welding clockwise in sequence 2, and welding counterpoint in sequence 3.

3.3. Simulation Results and Discussion

Figure 18 shows the colored maps of von Mises welding stresses in three different welding sequences. It can be seen that the overall distribution of the stress is basically the same in three different sequences. The main welding stress appears in the area near the welding joints of four poloidal segments, and the maximum stress value occurs at the centerline of welding joints. Meanwhile, the stress reduces with increasing distance to the centerline of the welding zone, and can almost be ignored in the zones away from the welding joints. In order to analyze the effect of the welding sequences on welding stresses further, Figure 19 provides the comparison of the maximum and average von Mises stresses obtained from a specific load (the black lines shown in Figure 18). As can be seen, the maximum stresses in sequence 1, sequence 2, and sequence 3 are 234.509 MPa, 234.731 MPa, and 234.508 MPa, respectively, and the average stresses are 117.268 MPa, 117.367 MPa, and 117.241 MPa, respectively. Hence, despite no obvious stress distribution difference in the three sequences, sequence 3 is more beneficial to control the welding stress than the other two sequences.

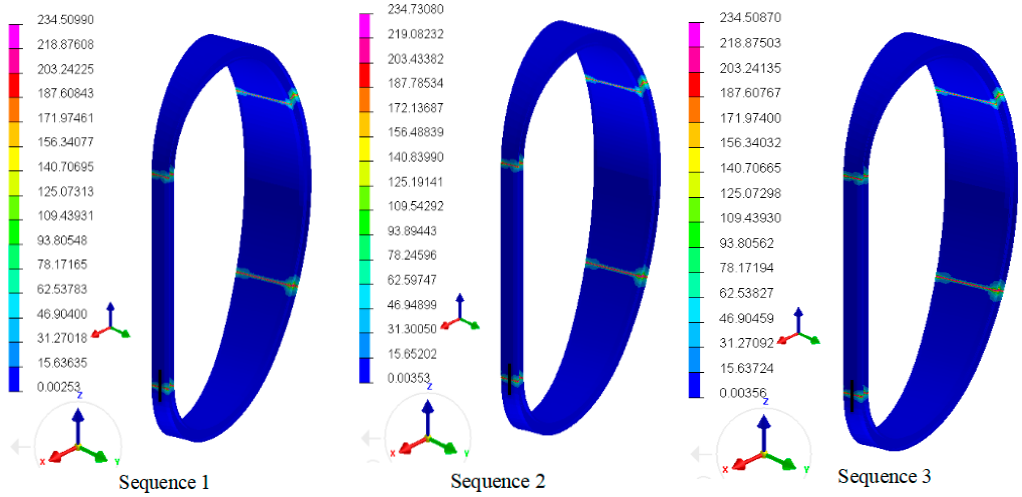

Figure 18. Colored maps of welding stresses in the three different sequences. The values on the left represent von Mises effective stress, different colors represent different stress values, and specific routes (black lines) were chosen at the same position in three sequences to analyze the effect of welding sequences on the welding stress concretely.

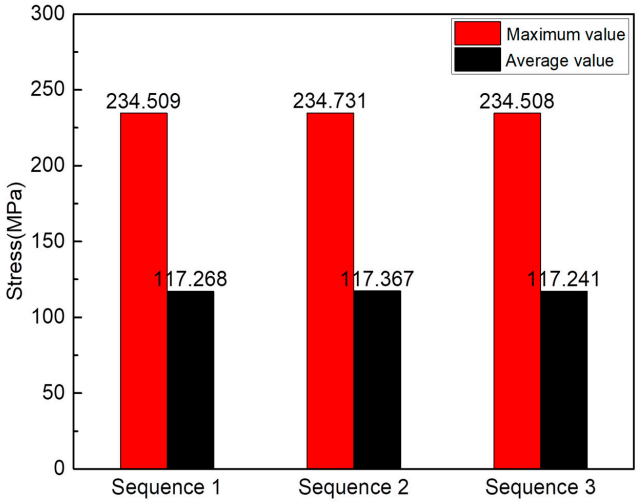

Figure 19. Comparison of the von Mises stresses according to the black routes (as shown in Figure 18) in three different sequences (the red histograms represent the maximum stresses, and the black ones represent the average stresses).

Figure 20 shows the colored maps of the welding distortion in the three different sequences. It can be seen that the distortion distributions in the three different sequences are similar. Figure 21 shows the overall distortion trends in the three different sequences before and after welding. As can be seen, PS1, PS2, and PS4 distort inward perpendicular to the shells, while PS3 distorts outward perpendicular to the shells. In order to investigate the influence of welding sequences on the welding distortions, a specific route (black line in Figure 20) on the outer shell was chosen to compare the maximum and average displacements between simulation and experiment. As Figure 22 shows, the maximum displacements in sequence 1, sequence 2, and sequence 3 are 1.158 mm, 1.157 mm, and 1.149 mm, respectively, and the average displacements are 1.048 mm, 1.053 mm, and 1.042 mm, respectively. Therefore, sequence 3 is more suitable for reducing welding distortion than the other sequences.

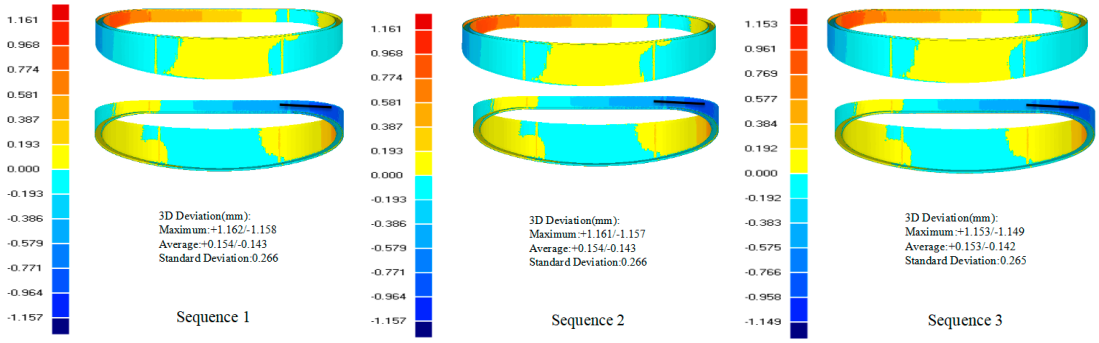

Figure 20. Colored maps of welding distortions in the three different sequence. The values on the left represent displacements, of which the positive values represent the outward distortion at outer shell and inward distortion at inner shell, and the negative values represent outward distortion at inner shell and inward distortion at outer shell. Specific routes (black lines) were chosen at the same position to analyze the effect of welding sequences on the welding stresses concretely.

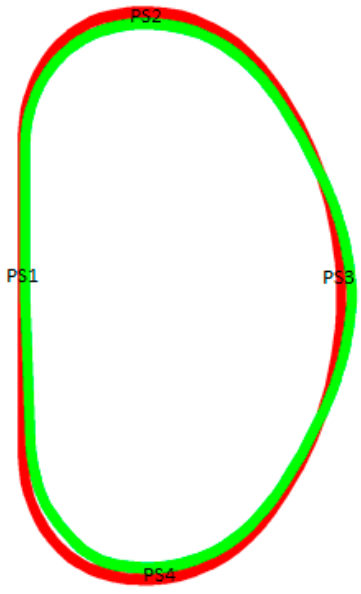

Figure 21. Overall distortion trends of the 1/32 VV mock-up in three difference sequences. Red line represents the initial shape before welding, and the green line represents the distorted shape after welding. PS1, PS2, and PS4 distort to inside perpendicular to the shells and PS3 distorts to outside perpendicular to the shells.

In summary, the overall distributions of the welding stresses and distortions both have no obvious difference in the three different welding sequences. This may be caused by the long distance between the welding joints, which eliminates the interaction between them. Besides, the strict constraints also

reduce the effect of welding sequences on the welding stress and distortion. It is worth noting that the maximum distortions all appear on the shell near the joint between PS1 and PS4, the reason may be that the starting points of welding are all at the joint between PS1 and PS2 in the three different sequences. However, according to the further comparison results at specific routes, sequence 3 can control the welding stresses and distortions more effectively than the other two sequences, and can be applied to the practical assembly process of the 1/32 VV mock-up.

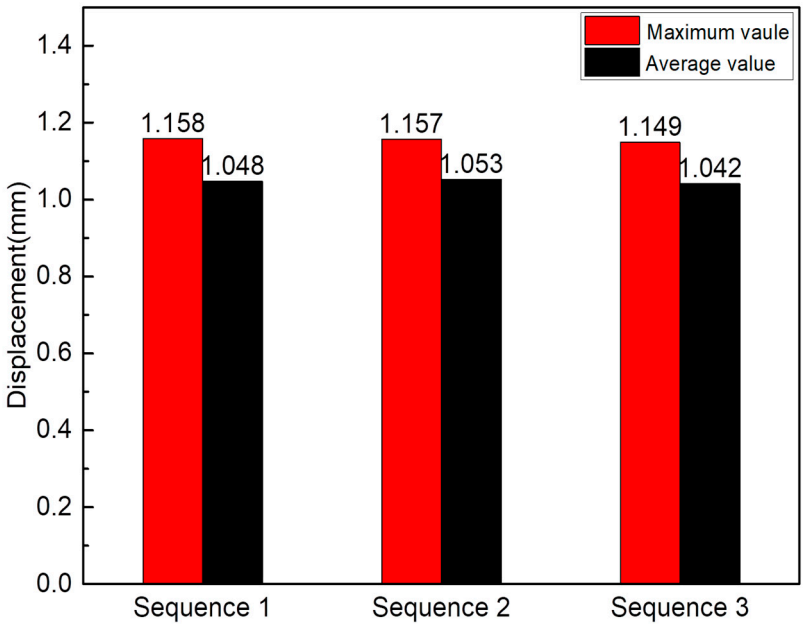

Figure 22. Comparison of the welding distortions according to the black route (as shown in Figure 20) in the three different sequences (the red histograms represent the maximum distortions, and the black ones represent the average distortions).

4. Conclusions

The influence of the welding sequences on the welding stress and distortion of the 1/32 VV mock-up was investigated using finite element simulation. The finite element model used in this study was adjusted and validated on the coupon, and the simulated results agreed well with experimental results. Then, the finalized finite element model was employed in the simulation of the 1/32 VV mock-up. In the simulation of the 1/32 VV mock-up, the overall distribution of the welding stresses and distortions both have no great difference in the three different sequences. The welding stress appeared at the welding joints in most cases, and could be ignored far away from the weld joints. As for the welding distortion, PS1, PS2, and PS4 distorted inward, while PS3 distorted outward. It was worth noting that the greatest distortion all happened on the shells near the welding joint between PS1 and PS4 in three sequences. According to the further analysis, the maximum stresses in sequence 1, sequence 2, and sequence 3, were 234.509 MPa, 234.731 MPa, and 234.508 MPa, respectively, the average stresses were 117.268 MPa, 117.367 MPa, and 117.241 MPa, respectively, while the maximum displacements were 1.158 mm, 1.157 mm, and 1.149 mm, respectively, and the average displacements were 1.048 mm, 1.053 mm, and 1.042 mm, respectively. Hence, sequence 3 was more beneficial to controlling the welding stresses and distortions than the other two sequences, and could be applied to the practical welding process of the 1/32 VV mock-up.

Author Contributions: Conceptualization, J.Z. and L.Y.; Methodology, J.Z. and L.Y.; Software, Z.L.; Validation, Y.L., H.L. and C.L.; Formal Analysis, J.Z.; Investigation, J.Z.; Resources, J.W. and J.M.; Data Curation, J.Z.; Writing-Original Draft Preparation, J.Z.; Writing-Review & Editing, J.Z. and L.Y.; Visualization, J.Z.; Supervision, L.Y.; Project Administration, L.Y.; Funding Acquisition, L.Y. and Z.M.

Acknowledgments: The authors are grateful to the International Thermonuclear Experimental Reactor (ITER) Program Special Project (No. 2015GB107003 and 2015GB119001), the National Nature Science Foundation of China (No. 51474155, 11672200, 51674175 and U1660201), and the Science and Technology program of Tianjin (No. 18YFZCGX00070) for grant and financial support.

Conflicts of Interest: The authors declare no conflicts of interest.

References

1. Liu, Z.; Wu, J.; Ma, J.; Fan, X.; Xiu, L. Study on the Welding Process of the Vacuum Vessel Mock-Up for CFETR. *IEEE Trans. Plasma Sci.* **2018**, *46*, 1608. [CrossRef]
2. Jones, L.; Arbogast, J.F.; Bayon, A.; Bianchi, A.; Caixas, J.; Facca, A.; Fachin, G.; Fernández, J.; Giraud, B.; Losasso, M.; et al. Manufacturing preparations for the European Vacuum Vessel Sector for ITER. *Fusion Eng. Des.* **2012**, *87*, 700–705. [CrossRef]
3. Caixas, J.; Guirao, J.; Bayon, A.; Jones, L.; Arbogast, J.F.; Barbensi, A.; Dans, A.; Facca, A.; Fernandez, E.; Fernández, J.; et al. Weld distortion prediction of the ITER Vacuum Vessel using Finite Element simulations. *Fusion Eng. Des.* **2013**, *88*, 2011–2014. [CrossRef]
4. Zhang, W.; Jiang, W.; Zhao, X.; Tu, S.-T. Fatigue life of a dissimilar welded joint considering the weld residual stress: Experimental and finite element simulation. *Int. J. Fatigue* **2018**, *109*, 182–190. [CrossRef]
5. Deng, D.; Murakawa, H.; Liang, W. Numerical simulation of welding distortion in large structures. *Comput. Methods Appl. Mech. Eng.* **2007**, *196*, 4613–4627. [CrossRef]
6. Chukkan, J.R.; Vasudevan, M.; Muthukumaran, S.; Kumar, R.R.; Chandrasekhar, N. Simulation of laser butt welding of AISI 316L stainless steel sheet using various heat sources and experimental validation. *J. Mater. Process. Technol.* **2015**, *219*, 48–59. [CrossRef]
7. Bachmann, M.; Avilov, V.; Gumenyuk, A.; Rethmeier, M. Experimental and numerical investigation of an electromagnetic weld pool support system for high power laser beam welding of austenitic stainless steel. *J. Mater. Process. Technol.* **2014**, *214*, 578–591. [CrossRef]
8. Ganesh, K.C.; Vasudevan, M.; Balasubramanian, K.R.; Chandrasekhar, N.; Mahadevan, S.; Vasantharaja, P.; Jayakumar, T. Modeling, Prediction and Validation of Thermal Cycles, Residual Stresses and Distortion in Type 316 LN Stainless Steel Weld Joint made by TIG Welding Process. *Proced. Eng.* **2014**, *86*, 767–774. [CrossRef]
9. Liu, C.; Zhang, J.X.; Xue, C.B. Numerical investigation on residual stress distribution and evolution during multipass narrow gap welding of thick-walled stainless steel pipes. *Fusion Eng. Des.* **2011**, *86*, 288–295. [CrossRef]
10. Perić, M.; Tonković, Z.; Rodić, A.; Surjak, M.; Garašić, I.; Boras, I.; Švaić, S. Numerical analysis and experimental investigation of welding residual stresses and distortions in a T.-joint fillet weld. *Mater. Des.* **2014**, *53*, 1052–1063. [CrossRef]
11. Vakili-Tahami, F.; Ziaei-Asl, A. Numerical and experimental investigation of T-shape fillet welding of AISI 304 stainless steel plates. *Mater. Des.* **2013**, *47*, 615–623. [CrossRef]
12. Lostado Lorza, R.; Escribano García, R.; Martínez Calvo, M.; Múgica Vidal, R. Improvement in the Design of Welded Joints of EN 235JR Low Carbon Steel by Multiple Response Surface Methodology. *Metals* **2016**, *6*, 205. [CrossRef]
13. Bonakdar, A.; Molavi-Zarandi, M.; Chamanfar, A.; Jahazi, M.; Firoozrai, A.; Morin, E. Finite element modeling of the electron beam welding of Inconel-713LC gas turbine blades. *J. Manuf. Process.* **2017**, *26*, 339–354. [CrossRef]
14. Kim, Y.C.; Hirohata, M.; Inose, K. FEM Simulation of Distortion and Residual Stress Generated by High Energy Beam Welding with Considering Phase Transformation. *Open J. Met.* **2014**, *04*, 31–39. [CrossRef]
15. Rong, Y.; Zhang, G.; Huang, Y. Study on deformation and residual stress of laser welding 316L T-joint using 3D/shell finite element analysis and experiment verification. *Int. J. Adv. Manuf. Technol.* **2016**, *89*, 2077–2085. [CrossRef]
16. Fu, G.; Lourenço, M.I.; Duan, M.; Estefen, S.F. Influence of the welding sequence on residual stress and distortion of fillet welded structures. *Mar. Struct.* **2016**, *46*, 30–55. [CrossRef]
17. Chen, Z.; Chen, Z.; Shenoi, R.A. Influence of welding sequence on welding deformation and residual stress of a stiffened plate structure. *Ocean Eng.* **2015**, *106*, 271–280. [CrossRef]

18. Sattari-Far, I.; Javadi, Y. Influence of welding sequence on welding distortions in pipes. *Int. J. Press. Vessel. Pip.* **2008**, *85*, 265–274. [CrossRef]
19. Deng, D. Influence of deposition sequence on welding residual stress and deformation in an austenitic stainless steel J-groove welded joint. *Mater. Des.* **2013**, *49*, 1022–1033. [CrossRef]
20. Guirao, J.; Rodríguez, E.; Bayón, A.; Cortizo, J.L.; Jones, L. A study of the influence of electron beam welding sequences on the ITER vacuum vessel prototype VATS. *Fusion Eng. Des.* **2011**, *86*, 2805–2811. [CrossRef]
21. Martín-Menéndez, C.; Rodríguez, E.; Ottolini, M.; Caixas, J.; Guirao, J. Analysis of the effect of the Electron-Beam welding sequence for a fixed manufacturing route using finite element simulations applied to ITER vacuum vessel manufacture. *Fusion Eng. Des.* **2016**, *104*, 84–92. [CrossRef]
22. Xiu, L.; Wu, J.; Liu, Z.; Ma, J.; Fan, X.; Ji, H.; Xia, X.; Li, Y. Weld distortion prediction of the CFETR vacuum vessel by inherent strain theory. *Fusion Eng. Des.* **2017**, *121*, 43–49. [CrossRef]
23. Fan, X.; Wu, J.; Liu, Z.; Gu, Y.; Ji, H.; Ma, J. Application of Contour Fitting Method in CFETR VV Assembly. *IEEE Trans. Plasma Sci.* **2018**, *46*. [CrossRef]
24. Ji, H.; Gu, Y.; Wu, J.; Liu, Z.; Fan, X.; Ma, J.; Xia, X. Reverse Engineering of CFETR Vacuum Vessel Mockup. *IEEE Trans. Plasma Sci.* **2018**, *45*. [CrossRef]
25. Hizli, H.; Gür, C.H. Comparison of Electronic Speckle Laser Interferometry Hole-Drilling and X-ray Diffraction Techniques for Determination of Residual Stresses in the Heat Treated Steels. *J. Nondestruct. Eval.* **2017**, *36*. [CrossRef]
26. Oliveira, J.P.; Fernandes, F.M.B.; Miranda, R.M.; Schell, N.; Ocaña, J.L. Residual stress analysis in laser welded NiTi sheets using synchrotron X-ray diffraction. *Mater. Des.* **2016**, *100*, 180–187. [CrossRef]
27. Lorza, R.L.; Bobadilla, M.C.; Calvo, M.A.M.; Roldán, P.M.V. Residual Stresses with Time-Independent Cyclic Plasticity in Finite Element Analysis of Welded Joints. *Metals* **2017**, *7*, 136. [CrossRef]
28. Goldak, J.; Chakravarti, A.; Bibby, M. A New Finite Element Model for Welding Heat Sources. *Metall. Trans. B* **1984**, *15*, 299–305. [CrossRef]
29. Lorza, R.L.; García, R.E.; Martinez, R.F.; Calvo, M.A.M. Using Genetic Algorithms with Multi-Objective Optimization to Adjust Finite Element Models of Welded Joints. *Metals* **2018**, *8*, 230. [CrossRef]